

Tuning 2D Perovskite Passivation: Impact of Electronic and Steric Effects on the Performance of 3D/2D Perovskite Solar Cells

Zeynep Gozukara Karabag, Aliekber Karabag, Ummugulsum Gunes, Xiao-Xin Gao,* Olga A. Syzgenteva, Maria A. Syzgenteva, Figen Varlioglu Yaylali, Naoyuki Shibayama, Hiroyuki Kanda, Alwani Imanah Rafieh, Roland C. Turnell-Ritson, Paul J. Dyson,* Selcuk Yerci,* Mohammad Khaja Nazeeruddin,* and Gorkem Gunbas*

Surface passivation with 2D perovskites is a powerful strategy to achieve improved stability and performance in perovskite solar cells (PSCs). Various large organic cations have been successfully implemented, led by phenylethylammonium (PEA⁺) and its derivatives. However, systematic studies on large sets of cations to understand the effect of substituent position on 2D perovskite passivation and device performance are lacking. Herein, a collection of halogenated PEA⁺ iodide salts (*x*-XPEAI where *x*: *ortho* (*o*), *meta* (*m*), *para* (*p*), X: F, Cl, Br) are synthesized by a facile method and deposited on top of 3D perovskite. The 2D perovskite layer formation is confirmed by X-ray diffraction (XRD) and grazing-incidence wide-angle X-ray scattering analyses for all cations, regardless of the nature and position of the halogen. Density functional theory analysis reveals that lower formation energies and higher interfacial dipoles achieved by *m*-substituted cations are responsible for enhanced performance compared to their *o*- and *p*-counterparts. While the *m*-BrPEAI-treated device shows a champion efficiency of 23.42%, ($V_{OC}=1.13$ V, FF=81.2%), considering average efficiencies, stability, and reproducibility, the treatment with *m*-ClPEAI salt yields the best overall performance. This comprehensive study provides guidelines for understanding the influence of large cation modification on performance and stability of 3D/2D PSCs.


1. Introduction

The search for low-cost, efficient, and stable solar technology has been central to energy research and development over the last three decades. The best research cell efficiency chart demonstrates how 3D hybrid perovskite solar cells (PSCs) have dominated the field in the last decade, owing to their excellent optoelectronic properties.^[1] Additionally, perovskites have demonstrated immense potential to be utilized in silicon/perovskite tandem solar cells to achieve efficiencies over the Shockley-Queisser limit for single junction devices, paving the way for unheard lows in the leveled cost of electricity.

The conventional cubic 3D perovskite structure is formed by the combination of three different components with a general formula ABX₃, where A is an organic/inorganic cation such as formamidinium iodide (FAI), methylammonium iodide (MAI) or cesium (Cs), B is a

Z. Gozukara Karabag, A. Karabag, U. Gunes, F. Varlioglu Yaylali, S. Yerci, G. Gunbas
ODTU-GUNAM
Middle East Technical University
Ankara 06800, Turkey
E-mail: syerci@metu.edu.tr; ggunbas@metu.edu.tr

Z. Gozukara Karabag, U. Gunes, X.-X. Gao, H. Kanda, A. I. Rafieh, R. C. Turnell-Ritson, P. J. Dyson, M. K. Nazeeruddin
Institute of Chemical Sciences and Engineering
Swiss Federal Institute of Technology Lausanne (EPFL)
Lausanne CH-1015, Switzerland
E-mail: xiaoxin.gao@epfl.ch; paul.dyson@epfl.ch; mdkhaja.nazeeruddin@epfl.ch
Z. Gozukara Karabag, G. Gunbas
Department of Chemistry
Middle East Technical University
Ankara 06800, Turkey
A. Karabag, F. Varlioglu Yaylali, G. Gunbas
Department of Polymer Science and Technology
Middle East Technical University
Ankara 06800, Turkey

 The ORCID identification number(s) for the author(s) of this article can be found under <https://doi.org/10.1002/aenm.202302038>

© 2023 The Authors. Advanced Energy Materials published by Wiley-VCH GmbH. This is an open access article under the terms of the Creative Commons Attribution-NonCommercial License, which permits use, distribution and reproduction in any medium, provided the original work is properly cited and is not used for commercial purposes.

DOI: 10.1002/aenm.202302038

metal cation (typically Pb^{2+}), and X is a halide anion (i.e., Cl^- , Br^- , I^-). The cubic 3D perovskite structure reveals excellent photovoltaic performance due to its high absorption coefficient, tunable band gap by halide substitution, low exciton binding energy ($\approx 10\text{--}50$ meV), easy photo-generation of free charges, long carrier diffusion length (0.1–1 μm), low trap density, and low non-radiative recombination rate, resulting in power conversion efficiencies (PCEs) exceeding 25%, comparable to their silicon counterparts.^[2–4] Additionally, the perovskite structure can be realized through straightforward, low-cost processes resulting in high crystallinity materials.^[5] While the short-circuit current density (J_{SC}) and fill factor (FF) of PSCs are already close to their theoretical limits (≈ 26 mA cm^{-2} and 88% for a band gap of 1.55 eV), recent studies have been mainly focused on the improvement of the open-circuit voltage (V_{OC}) of PSCs.^[6]

Unfortunately, the lack of long-term stability hinders the anticipated commercialization of PSCs. Conventional 3D PSCs are liable to degradation from extrinsic factors such as moisture, temperature, and UV light, as well as intrinsic ones, including ion migration and interface defects.^[7] Low-dimensional 2D perovskites are more stable than their 3D counterparts due to the introduction of larger hydrophobic organic groups in the crystal structure, which not only improve water tolerance but also suppress ion migration.^[8] However, 2D perovskites lack efficient charge transport due to the presence of an insulating organic layer and display poor light absorption owing to their high band gap.^[9] Additionally, these materials tend to possess high exciton binding energy, resulting in diminished charge extraction to the transport layers.^[10] To combine the advantages of both 3D and 2D perovskites into a single device, 2D perovskite films are employed on the surface of 3D perovskite films to enhance stability without compromising PCE. Recently, it has been demonstrated that in addition to improved stability, performance enhancement can be achieved in 3D/2D perovskites.^[11]

Different types of bulky organic cations have been widely reported in the literature and used for different purposes (i.e., 2D PSCs,^[12] interfacial passivation layer(s) on bottom and/or top of 3D perovskite^{[13],[14]} or 3D/2D PSCs^[15]) to fabricate highly stable and efficient PSCs over the last decade. Among

them, multi-functional halogen-containing phenylalkylammonium cations (XPA^+A^+ ; X: F, Cl, Br; P: phenyl; A^{*}: alkyl chain either methyl or ethyl; A: ammonium) have a great reputation to develop high-performing PSCs via introducing these cations as either 2D Ruddlesden-Popper (RP) layer or interfacial protective layer on top of 3D perovskite. Gao et al. introduced the 2D layer formed by 2-(2-fluorophenyl)ethylamine iodide (*o*-FPEAI), 2-(3-fluorophenyl)ethylamine iodide (*m*-FPEAI), and 2-(4-fluorophenyl)ethylamine iodide (*p*-FPEAI) atop their 3D perovskite to construct 3D/2D PSCs and reported over 20% PCE with improved stability under continuous illumination for 1440 h.^[16] In 2019, You et al. reported the fabrication of only 2D PSCs using a set of mono-fluorinated PEAI salts, namely *o*-FPEAI, *m*-FPEAI, and *p*-FPEAI.^[17] With respect to the control device based on PEAI salt (7.67% PCE), the photovoltaic device efficiencies were improved by over 10% upon utilization of *m*-FPEAI (10.17%) and *p*-FPEAI (10.55%) salts. In the case of *o*-FPEAI-treated 2D PSC, the device efficiency drastically decreased to 0.50%. Among these 2D PSCs, non-encapsulated *m*-FPEAI-based 2D PSC showed the highest stability under 45% humidity at room temperature for 30 days.

You and Liu et al. have examined the effect of molecular polarity on the performance of 3D/2D PSCs using fluorinated 2D-forming salts, namely *o*-FPEAI and (2-fluorophenyl)methylammonium iodide (*o*-FPMAI).^[18] They reported that between the *o*-FPEA⁺ and *o*-FPMMA⁺ cations, the longer carbon chain resulted in a reduced inductive effect between amino and fluorine units. Hence, there is a larger dipole for *o*-FPEAI than *o*-FPMAI, which results in better band alignment and charge transport at the interface. The authors also indicated that the significant molecular polarity enhances the passivation effect by improving the interactions between the 2D passivator and the PbI_2 , enabling a device performance higher than 23% PCE with an impressive V_{OC} of 1.16 V and FF of 81.36%. The cells retained 82.5% of the initial PCE with high stability for 2000 h at 40% relative humidity and room temperature. In 2021, a set of fluorinated PEAI salts (*o*-FPEAI, *m*-FPEAI, and *p*-FPEAI) on 3D perovskite film were employed as a direct passivation layer instead of forming a 2D perovskite layer. These salts improved the efficiency and long-term stability at a relative humidity of 15–25% after 430 h. The *meta*-substituted FPEAI-treated PSC gave an efficiency of over 23%.^[19]

Besides fluorine substitution, chlorine, and bromine substitution on the phenyl ring of the PEA^+ cation has also been reported to have an impact on the performance of the resulting devices. Liu, Xing, Zhao, and Zheng et al. examined the effect of F, Cl, and Br substitution on the crystal orientation and phase distribution of the quasi-2D (Q-2D) RP perovskite films.^[20] Q-2D RP PSC based on (*p*-FPEA)₂MA₃Pb₄I₁₂ ($n = 4$) was reported to demonstrate higher efficiency of 18.10% than that of (PEA)₂MA₃Pb₄I₁₂ (12.23%), (*p*-ClPEA)₂MA₃Pb₄I₁₂ (7.93%) and (*p*-BrPEA)₂MA₃Pb₄I₁₂ (6.08%) structured counterparts and also exhibited greater stability after aging 30 days with relative humidity (RH) of 40–50% at room temperature.^[21] The reports showed primarily that the addition of electron-withdrawing halogen substituents to the phenyl ring of PEAI salts induces higher polarity, leading to lower exciton binding energy and more effective exciton dissociation in the 2D-perovskite structures.^[21–23] Several other critical works related to halogen-substituted phenyl

U. Gunes, S. Yerci, G. Gunbas
Department of Micro and Nanotechnology
Middle East Technical University
Ankara 06800, Turkey

O. A. Syzgenteva
Department of Chemistry
Lomonosov Moscow State University
Moscow 119991, Russia

M. A. Syzgenteva
Department of Physics
Mendeleev University of Chemical Technology
Moscow 125047, Russia

N. Shibayama
Department of General Systems Studies
Graduate School of Arts and Sciences
The University of Tokyo
3-8-1 Komaba, Meguro-ku, Tokyo 153-8902, Japan

S. Yerci
Department of Electrical and Electronics Engineering
Middle East Technical University
Ankara 06800, Turkey

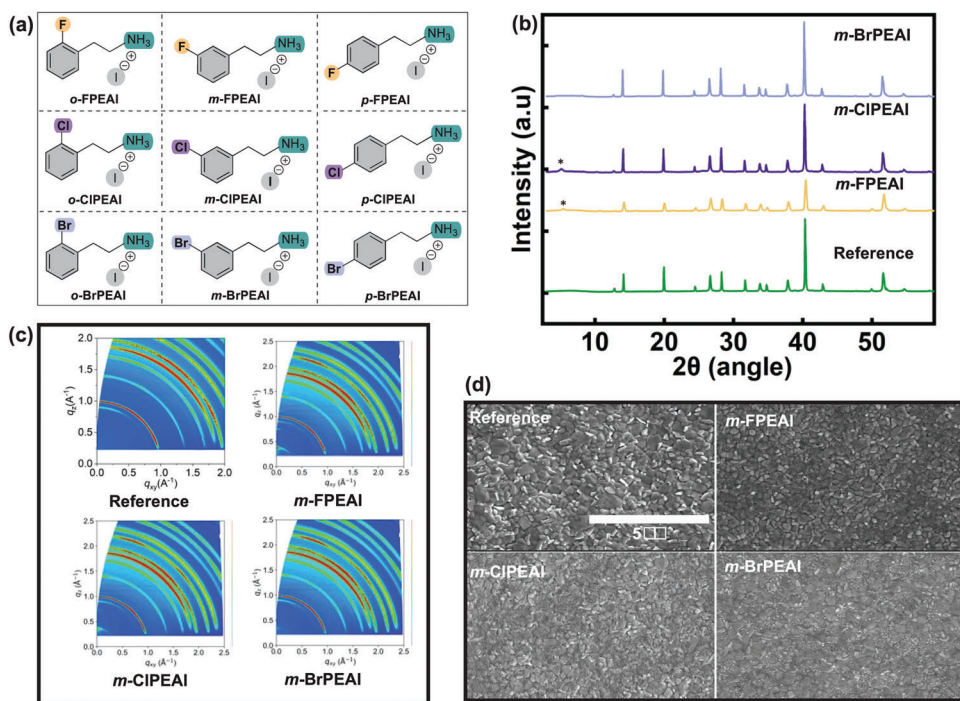


Figure 1. a) Structures of the nine different halogenated PEAI salts synthesized and used in this study; b) XRD patterns of *m*-XPEAI-treated perovskite films; c) GIWAXS images (with 2.0° incident angle); and d) SEM images of the reference and meta-substituted salt-treated 3D perovskite films.

alkylammonium iodide salts are given in detail (Table S1 and Figure S1, Supporting Information).^[24–37]

Despite the large number of studies exploring the effect of PEAI-type salts on the performance of PSCs in the literature, detailed systematic analysis and a fundamental understanding of the nature (electronic effects), the size, and the position (steric effects) of the substituents of 2D-perovskite-forming salts on the performance of 3D/2D PSCs is lacking.^[38] We recently demonstrated the positional effect of methoxy (-OMe) substituents on the orientation of 2D-forming PEAI salts (*x*-OMe-PEAI salts (*x* = *o*, *m*, *p*)) on 3D/2D perovskite films.^[39] In the present work, a series of bulky organic cations based on the phenylethylammonium (PEA) framework with 3 different halogens (F, Cl, and Br) that vary significantly in their size and electronegativity were realized. For all halogens, the substituent position also varied (*ortho* (*o*), *meta* (*m*), and *para* (*p*)) positions) on the aromatic ring, yielding nine different *x*-XPEAI salts (*x* = *o*, *m*, *p*; X = F, Cl, Br) toward understanding the effect of electronics and sterics on the performance of resulting 3D/2D perovskite solar cells. The salts were deposited on the surface of CsFAMA-based 3D triple cation perovskites and we successfully demonstrated the formation of 2D perovskite layers for all 9 salts via X-ray diffraction (XRD) and grazing incident wide-angle X-ray scattering (GIWAXS) analyses. Photoluminescence (PL) and time-resolved photoluminescence (TRPL) spectroscopy results showed that a 2D perovskite layer based on *m*-XPEA₂PbI₄, suppresses nonradiative carrier recombination more effectively than both its *ortho* or *para*-analogs and the untreated reference. Among these nine different 2D perovskites, *m*-XPEA₂PbI₄ had higher interfacial dipoles and lower formation energies on the 3D perovskite surface, as demonstrated by detailed DFT analyses. While halogen substitution at

the *meta*-position of the phenyl ring of 2D PEAI salts results in higher V_{OC} (1.13 V) and FF (over 81%), furnishing an enhanced PCE exceeding 23% the identity of the halogen showed a limited effect. Hence, regarding halogen substitution in PEAI-based salts, we demonstrated that steric effects, which dictated the orientation and thus the surface dipole, are the basis for the enhanced performance. For clarity, data related to *meta*-substituted PEAI-based salts are shared in the main text, and data related to *ortho* and *para*-substituted counterparts are given in the supporting information.

2. Results and Discussion

The *o*-, *m*-, and *p*-halogenated phenylethylammonium cations (*x*-XPEA⁺) were synthesized by a robust and facile method in good yields (>80% over three steps; Figures S2 and S3, Supporting Information). For all device architectures, the [(Cs_{0.04}FA_{0.85}MA_{0.11})Pb(I_{0.96}Br_{0.01}Cl_{0.03})₃]-based triple cation 3D perovskite composite was utilized and deposited via the traditional spin coating method. The synthesized *x*-XPEAI salts were individually coated on top of the 3D perovskite to construct 3D/2D hybrid structures using the same method. The chemical structures of each *x*-XPEAI-based salt are represented in Figure 1a.

XRD diffraction patterns of the *m*-XPEAI salt-treated 3D perovskites are shown in Figure 1b, as well as the untreated 3D perovskite as a reference. XRD peaks lower than 10° (2θ) are typically assigned to 2D perovskite crystals.^[40] The observed 2D peaks are located at 5.13° and 5.40°, indicating the formation of the {002} plane of the 2D ($n = 1$) films^[7,41,42] for *m*-CIPEAI and *m*-FPEAI, respectively, which are consistent with XRD peaks of

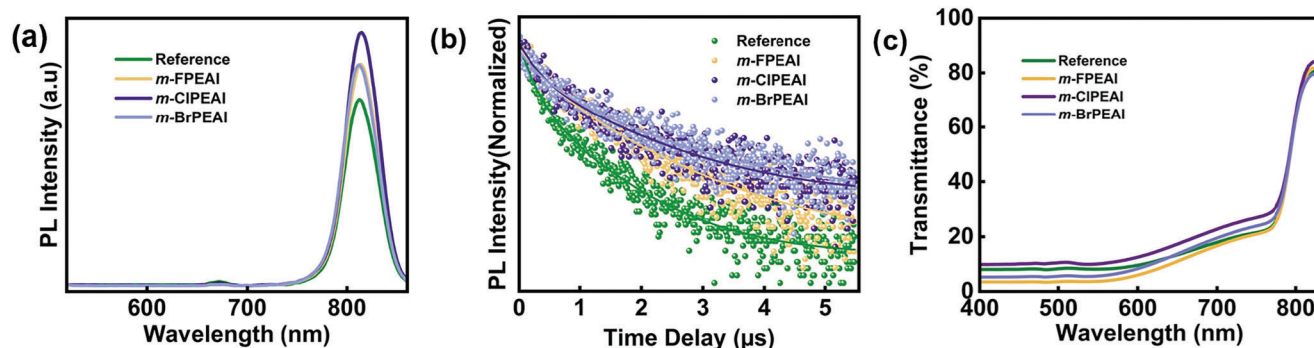


Figure 2. a) Steady-state photoluminescence spectra; b) Time-resolved PL traces; c) Transmission spectra of reference and *meta*-halogenated PEAI salt-treated 3D perovskite films.

the pure 2D ($n = 1$) material (5.16° and 5.33° for *m*-CIPEAI and *m*-FPEAI, respectively; S4, Supporting Information). The 3D perovskite film (reference) has a PbI_2 peak around 12.6° , which almost disappears after treatment with *m*-XPEAI salts. This suggests that the organic ammonium salts react with excess PbI_2 on the surface of 3D perovskite to form a 2D layer.^[43] GIWAXS measurements were performed to investigate the orientation of the 2D films on the 3D perovskite with three different incident angles: 0.12° , 0.4° , and 2.0° (Figures S5–S7, Supporting Information). GIWAXS images, performed with an incident angle of 2.0° for the *m*-XPEAI-doped 2D films and the reference, are shown in Figure 1c. The corresponding Debye-Scherrer rings at $q_z = 1.0 \text{ \AA}^{-1}$ and $q_z = 0.9 \text{ \AA}^{-1}$ represent the preferential orientation for the $\{110\}$ crystal plane of 3D perovskite and $\{001\}$ crystal plane of PbI_2 , respectively.^[44,45] For all the GIWAXS films, there is a decrease in the PbI_2 peak at $\{001\}$ crystal plane with the inclusion of halogenated salts, which indicates the reaction of PbI_2 with PEAI salts.^[46] As a result, a new spot appears below $q_z = 0.5 \text{ \AA}^{-1}$ for all the salt-treated films, which refers to the formation of the 2D perovskite layer. The Bragg spots in a low incident angle measurement (0.12°), which is more surface sensitive, show strong preferential orientation for the nine 2D films on the surface where the 2D perovskite films are oriented parallel to the substrate (Figure S5, Supporting Information).^[47] As the incident angle increases, 2D perovskite Debye-Scherrer rings weaken, and the rings related to 3D perovskite films with a random orientation become more obvious, proving that the 2D films are formed on the surface of the 3D film.^[48,49]

Top-view scanning electron microscopy (SEM) studies were performed to investigate the morphology of the perovskite films, with and without the addition of halogenated PEAI salts (Figure 1d; Figure S8, Supporting Information). As shown in Figure 1d, the reference film displays significant white contrast at the grain boundaries, which is generally attributed to the presence of excess PbI_2 on 3D perovskite films.^[50–52] After treatment with *meta*-halogenated PEAI salts, the white PbI_2 flakes decrease on the films, which further proves the reaction between the PbI_2 and ammonium salts.^[53] Cross-section SEM images of all 3D/2D films are given in Figure S9 (Supporting Information). 2D films are not visible on top of 3D perovskite films due to their extremely thin nature.^[54] Atomic force microscopy (AFM) images of 3D and 3D/2D films are shown in Figure S10 (Supporting Information). The formation of all the 2D layers results in smoother surfaces

than the reference film, as given by the lower root mean square (RMS) values of the films generated from the addition of the *meta*-halogenated ammonium salts, *m*-FPEAI, *m*-CIPEAI, and *m*-BrPEAI, are 18.18, 23.97, and 15.54 nm, respectively, while the RMS value for the reference film is 46.13 nm.

The optical properties of the reference film and *ortho*-XPEAI-treated perovskite films were investigated by PL, TRPL, and UV-vis spectroscopy (Figure 2a–c). PL measurements were performed using a 450 nm excitation from the film side. The greater PL intensity of the 2D treated 3D films, located at 812 nm, was observed when compared with the reference film, which is commonly associated with decreased nonradiative recombination.^[55] There is no PL emission from 2D perovskites at shorter wavelengths due to the low concentration of 2D precursor solutions; thus, highly thin films are produced in the process (Figure 2a).^[56] In correlation, the PL spectra of all the salt-treated films are shown in Figure S11d–f (Supporting Information), among which the *meta* positions have the most enhanced PL intensity of all halogen substituents. This demonstrates that suppression of nonradiative carrier recombination is superior in *meta*-substituted XPEAI derivatives. The average carrier lifetime in the 3D/2D perovskite film is significantly longer compared to the reference device, as shown by the TRPL spectra (Figure 2b). It is envisioned that 2D perovskite films reduce defect density, thereby decreasing nonradiative recombination. The carrier lifetimes are calculated from the TRPL spectra, and data are given in Table S2 (Supporting Information). All the halogenated salts treated perovskites have longer carrier lifetimes than the reference film, confirming the suppressed nonradiative recombination and enhanced defect passivation, thereby increasing V_{OC} .^[57] Among these nine salts, the *meta*-halogenated derivatives show longer lifetimes than their *ortho* and *para* counterparts. The UV-vis transmission data demonstrate that placing a 2D layer on top of the 3D perovskite does not affect the transmittance of the 3D/2D hybrid structure (Figure 2c; Figure S12a–c, Supporting Information).

The perovskite solar cells with and without 2D layers were fabricated and characterized under 1 sun illumination. Remarkable improvements in V_{OC} (in the absence of band gap change with the salt treatment) and FF (together with reduced series resistance) were observed in salt-treated 3D perovskite films, indicating superior surface passivation and enhanced hole extraction, respectively, as shown in Figure 3a,b and Figure S13

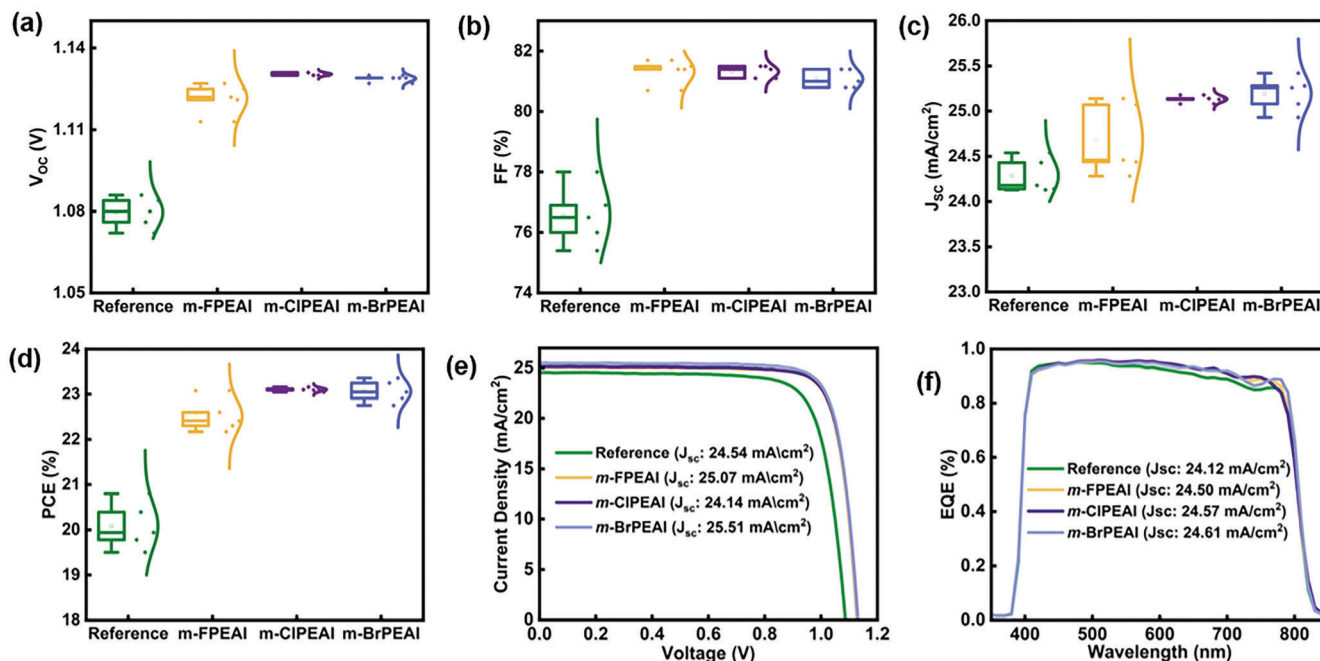


Figure 3. a–d) Statistics of reference and 3D/2D films; e) $J-V$ Curves of the pristine and halogenated PEAI treated devices simulated under 1 sun illumination; f) EQE spectra and calculated photocurrent values.

(Supporting Information).^[58,59] The increase in the J_{SC} for salt-treated films (Figure 3c) results in enhanced PCE (Figure 3d), and absorption in 3D perovskite is not increased by the very thin 2D films. The detailed device parameters for all salts are outlined in Table S3 and Figure S14 (Supporting Information). 2D passivated films show lower hysteresis than the reference film, indicating reduced ion migration and enhanced charge extraction.^[60–63] The reference 3D device showed a maximum PCE of 20.80%, with a V_{OC} of 1.09 V, a J_{SC} of 24.54 mA cm⁻², and an FF of 79.7% lower in all cases compared to the 3D/2D counterparts. The device performance is significantly improved by the introduction of 2D layers on top of 3D perovskite films. The average V_{OC} for the 3D/2D PSCs is around 1.13 V, which implies that the formation of 2D layers by α -XPEAI salts effectively passivates the recombination centers.^[64] Better device parameters are observed by inserting the m -XPEAI 2D layer (PCE: >23%), consistent with PL and TRPL studies. The integrated J_{SC} from the external quantum efficiency (EQE) measurements aligns with the J_{SC} from the current density-voltage ($J-V$) curve in Figure 3e,f.

Figure 4 shows the optimized structures for the 2D cations on the 3D perovskite surface. The formation energies of the (α -XPEA)₂PbI₄ layers are calculated by DFT calculations (Table S4, Supporting Information). It is shown that the formation energy of (m -FPEA)₂PbI₄, (m -CIPEA)₂PbI₄, and (m -BrPEA)₂PbI₄ on 3D perovskite films is lower than the 2D perovskites formed from *ortho* or *para*-substituted XPEAI salts. This lower formation energy correlates with the observed high device performances with m -XPEAI salts. With more favorable formation energy, forming large domains that result in a more compact film is relatively easier.^[17] The interfacial dipole of the 3D/2D interface is determined using DFT calculations, and the 3D layer treated with 2D

(m -XPEA)₂PbI₄ perovskite forms a surface with a higher interfacial dipole (Table S5, Supporting Information). This result is consistent with our device performance data, indicating that higher interfacial dipole implies better hole extraction from perovskite to hole transport layer.^[16] The position of halogen atoms on the phenyl ring affects the strength of the σ -electron withdrawing inductive effect, the π -electron resonance, and the molecular dipole moment. The combination of the first two of these parameters can be estimated from the Hammett parameters, σ_{meta} and σ_{para} , given in Table 1. These parameters are calculated from the effect of *meta* and *para* substituents on the pK_a of substituted benzoic acid, relative to the unsubstituted acid. The σ_{meta} parameter indicates the electron-withdrawing power of the substituent, as no resonance structure adds (or removes) significant electron density onto the *ipso* carbon. The three halogen atoms all display very similar net inductive effects in the *meta* position. The σ_{para} parameter, on the other hand, is affected by π donation due to resonance, and this effect is much greater for F than Cl or Br. As the *ortho* position has similar resonance structures to the *para* position, but with slightly stronger negative induction due to proximity, a theoretical " σ_{ortho} " parameter (which cannot be experimentally determined due to steric effects) would be expected to have slightly more positive values than σ_{para} . It can therefore be seen

Table 1. Hammett parameters for halogen substituents.^[65]

Halogen Substituent	σ_{meta}	σ_{para}
F	+0.34	+0.06
Cl	+0.37	+0.23
Br	+0.39	+0.23

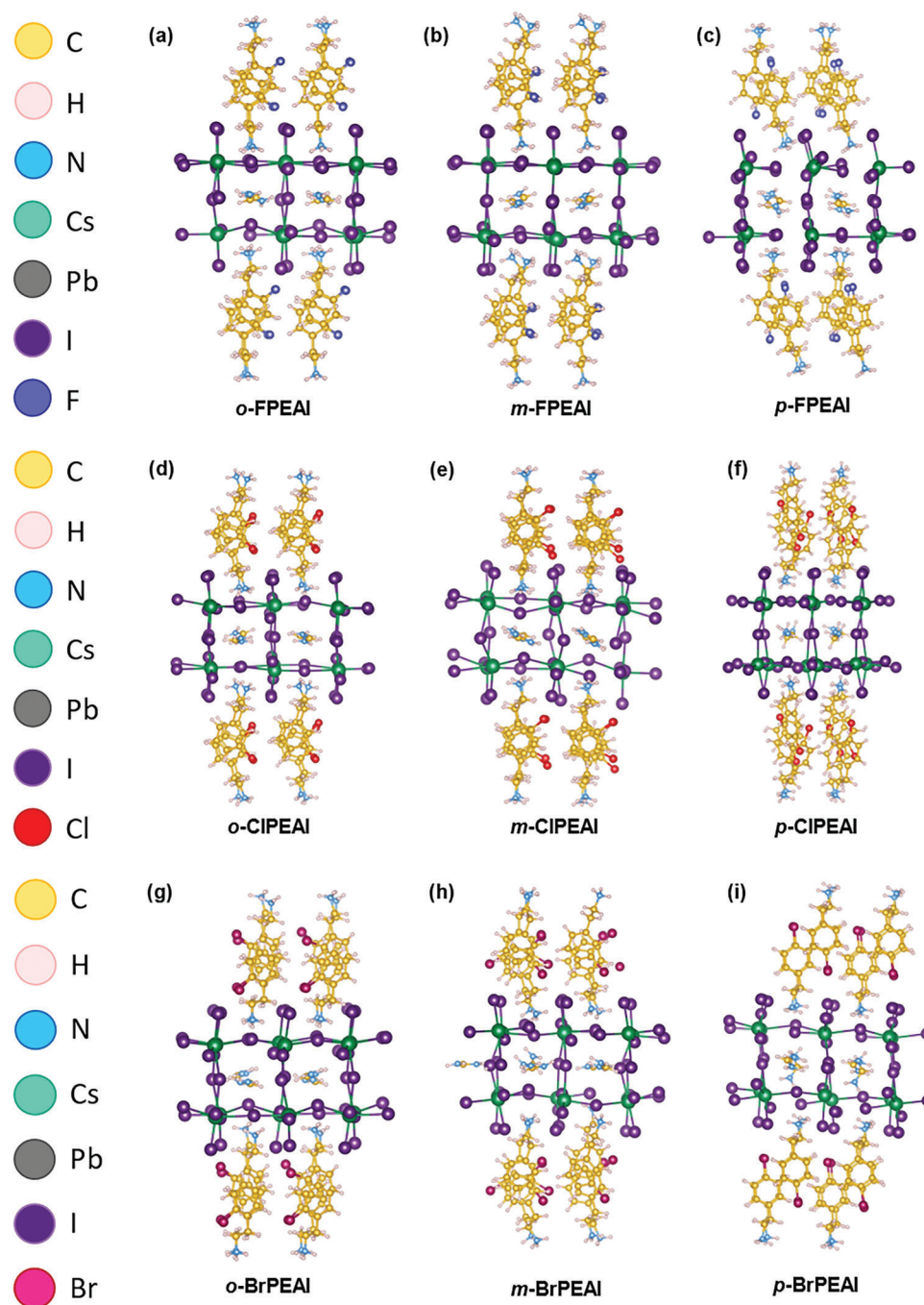


Figure 4. Theoretical modeling of all the halogenated salts at three different positions by DFT analysis.

clearly that halogen substituents in the meta position are most strongly electron-withdrawing.

From the *ortho* to *para* position on the phenyl ring, the molecular dipole increases. The combination of electron distribution and the molecular polarity from the dipole moment results in a better passivation effect of the $(m\text{-XPEA})_2\text{PbI}_4$ 2D layer.^[19] Furthermore, there is another structural factor affecting the performance. The formation of a 2D perovskite layer with $x\text{-XPEA}^+$

cations affects the structure of PbI_2 layers differently. *Ortho* and *para* substituents cause the highest disruption of the PbI_6 octahedral network, as compared to *meta*-substituted XPEA^+ . For *ortho*-substituted analogs, this disruption is expressed in the significant elongation of inter-octahedral connections in the *ac* plane. For *para*-substituted analogs, the Pb–I bond breakage is observed in the *ac* and *bc* planes. In the *meta*-substituted cases, the distribution of bonds is the most homogeneous, which should result in

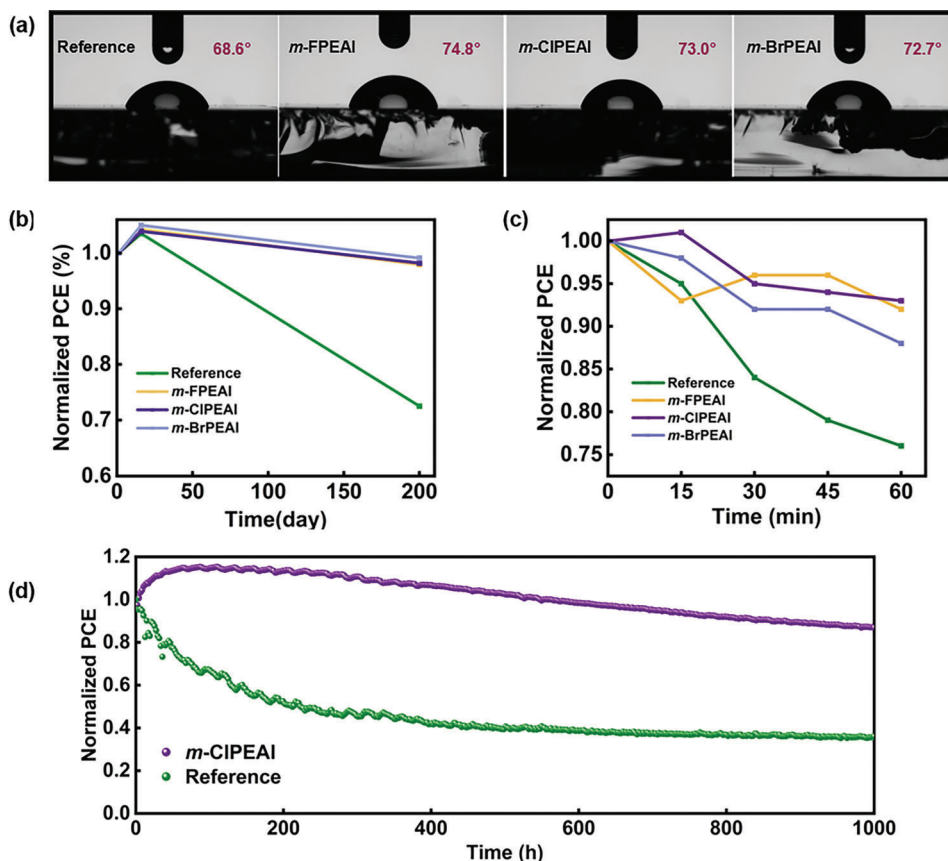


Figure 5. Comparison between the reference 3D perovskite and *m*-XPEAI-treated 3D/2D films on: a) contact angle of a surface water droplet; b) ambient air stability (RH > 20%, T = 20–25 °C); c) thermal stability (RH = 60–70%, T = 60 °C); and d) long-term stability of unencapsulated *m*-CIPEAI-treated and reference device at maximum power point (MPP) tracking under continuous 1-sun illumination and nitrogen atmosphere.

the best polaronic mobility and conductivity, and hence higher PSC performance (Figure 4a-i; Figure S15, Supporting Information).

In addition to the static structural analysis, we have performed ab initio molecular dynamics simulations of the α -XPEAI cation behavior on the FAI- and PbI₂-terminated (001) surfaces of FAPbI₃ to unravel the possible interaction and passivation features as a function of organic cation structure and composition. Using this technique, it was observed that the *m*-CIPEAI cation has the most favorable configuration to interact through the halide atom with the surface, passivating under-coordinated Pb²⁺ cations. This contrasts with the *p*-CIPEAI cation, which keeps a vertical orientation upon interacting with both types of surfaces. As for the *o*-CIPEAI cation, the *ortho*-Cl hampers the bending of the molecule, responsible for the simultaneous halogen and amino-group interaction. The same scheme applies to all other *ortho*-substituted analogies. The resulting *meta*-passivation, in particular, prevents the disruption of the Pb–I–Pb connection due to the migration of the I to the superficial position. In contrast, such migration is observed for the *o*-BrPEAI, *o*-FPEAI, and *p*-BrPEAI, resulting in a disconnection of the octahedral chains. *p*-FPEAI mainly interacts via NH₃-groups with little interaction of the substituted benzene ring with the perovskite surface. These observations from ab initio molecular dynamics (MD) simula-

tions correlate with the highest observed performance of the *m*-CIPEAI structures.

Contact angles of the reference and *meta*-halogenated salt-treated perovskite films with water are also measured, as shown in Figure 5a. 3D/2D films exhibit more hydrophobic surfaces than the control 3D perovskite film due to the nature of the *m*-XPEAI salts, which are oriented so that the organic part of the molecule points away from the surface (Figure 4). An ambient air stability test was performed for all nine salt-treated and reference devices. Non-encapsulated devices were kept in a dry box with relative humidity (RH) of over 20% for 200 days at 20–25 °C (Figure 5b; Figure S16, Supporting Information). The *m*-XPEAI-treated 3D/2D devices (Figure 5b) showed superior ambient stability (average 98% of their original performances) compared to the control device (73% of its original performance). For the thermal stability test, non-encapsulated *m*-XPEAI-treated devices were kept in a glove box with a RH of 60–70% for 60 min at 60 °C (Figure 5c). All 3D/2D devices, containing only *m*-XPEAI salts (Figure 5c) demonstrated greater thermal stability (average 91% of their original performances) compared to the control device (76% of its original performance). In order to get more reliable data, the photostability test under continuous 1-sun illumination was also conducted based on the overall best-performing PEAI-based salt (*m*-CIPEAI) among α -XPEAI family and the reference

device (Figure 5d). Both PSC devices were maintained in a nitrogen atmosphere under a constant illumination of 100 mW cm^{-2} . The current density-voltage ($J-V$) curves were recorded every 2 h. After 1000 hours of continuous illumination, the MPO (maximum power output) of the *m*-CIPEAI-treated device exhibited enhanced long-term stability (87% of its original performance) compared to the reference device (36% of its original performance). These results provide a clear perspective of the substantial benefit of our passivation materials, and pave the way toward molecular design of functional passivation materials.

3. Conclusion

In conclusion, we introduced nine different halogenated PEAI salts, namely *x*-XPEAI, on 3D perovskite films. Of these *x*-XPEAI salts, three (*o*-CIPEAI, *m*-CIPEAI, and *m*-BrPEAI) had not previously been tested in PSCs. Our findings reveal that the *meta*-substituted salts *m*-FPEAI, *m*-CIPEAI, and *m*-BrPEAI significantly improved the power conversion efficiency (PCE) of the 3D/2D devices, surpassing 23%. DFT calculations demonstrate that the 2D (*x*-XPEA)₂PbI₄ perovskites formed from *meta*-substituted *m*-XPEAI salts have a lower formation energy than their *ortho*- or *para*-substituted counterparts. Photoluminescence spectroscopy indicates an enhanced V_{OC} (1.13 V) and defect passivation on the 3D FAPbI₃ surface by the addition of a 2D (*m*-XPEA)₂PbI₄ perovskite layer. Based on our results, the effect of the substitution position is more pronounced than the identity of the halogen in device performance. Due to the orientation of the organic cation, the 2D layer formed by PEAI salts on top of the 3D perovskite film provides a hydrophobic surface, that significantly reduces moisture-induced degradation of the 3D perovskite layer. Among them, *m*-XPEAI-treated 3D films have shown superior thermal stability surpassing the reference device. After 1000 h continuous light exposure, the *m*-CIPEAI-treated 3D perovskite devices showed excellent photostability. Considering all aspects of efficiency, stability, and reproducibility, the treatment with *m*-CIPEAI salt yielded the best performance in 3D/2D perovskite solar cells. Overall, our study demonstrates the significant benefits of incorporating *meta*-substituted PEAI salts into 3D perovskite films, providing valuable insights for advancing perovskite-based solar cell technologies.

4. Experimental Section

Materials: Titanium dioxide paste (30NR-D), formamidinium iodide (FAI), and methylammonium bromide (MABr) were purchased from Greatcell Solar. Lead iodide (PbI₂) was purchased from Tokyo Chemical Company (TCl). Titanium diisopropoxide bis-(acetylacetonate) solution (75% in IPA), *spiro*-OMeTAD, bis(trifluoromethane)sulfonimide lithium salt (Li-TFSI), 4-*tert*-butylpyridine (*t*-BP), and chlorobenzene (CB) were provided from Sigma Aldrich. Isopropyl alcohol (IPA, 99.8%), SnCl₄ aqueous (99%), dimethylformamide (DMF, 99.9%), and dimethyl sulfoxide (DMSO, 99.9%) were purchased from Acros Organics.

Solar Cell Fabrication: The FTO glass substrates (TEC9AX) were cleaned with detergent, deionized water, acetone, and isopropanol by ultrasonication for 10 min, respectively. The cleaning procedure was followed by the UV-ozone treatment of substrates for 10 min. The compact TiO₂ (*cp*-TiO₂) was deposited onto the clean FTO substrates by spray pyrolysis using a titanium diisopropoxide bis-(acetylacetonate) solution diluted in IPA at 1:15 volume ratio on 450 °C and followed by in situ an-

nealing for 30 min. The mesoporous TiO₂ (*mp*-TiO₂) solution was composed of 1 g of TiO₂ paste diluted in 10 mL of anhydrous ethanol solution; then, the *mp*-TiO₂ layer was deposited onto the FTO/*cp*-TiO₂ substrate by a one-step spin-coating process at 4500 rpm for 20 s. After annealing at 125 °C for 30 min, the *mp*-TiO₂ films were gradually heated to 500 °C in air, and then, they were baked at the same temperature for 20 min to remove organic components. SnO₂ layers were prepared by spin coating 0.1 M SnCl₄ aqueous solution by a one-step process at 3000 rpm for 20 s; then, the substrates were transferred onto a hot plate and heated between 150 and 190 °C for 1 h. Before use, the FTO/*cp*-TiO₂/*mp*-TiO₂/SnO₂ substrates were treated with UV/ozone for 30 min. The precursor solution was prepared by dissolving PbI₂ (1.35 M), CsI (0.05 M), FAI (1.12 M) MABr (0.05 M), and MACl (0.10 M) in a mixed solvent of DMF: DMSO (4:1, volume ratio). Then, 25 μL perovskite precursors were coated onto the FTO/*cp*-TiO₂/*mp*-TiO₂/SnO₂ substrates (around 1.4 cm \times 2.4 cm) by spin-coating; the procedure was performed through a two-step program running at 1000 and 4000 rpm for 12 and 25 s, respectively. During the second step, 750 μL of CB as an anti-solvent was dropped quickly onto the center of the substrates after 11 s into the second step was dispensed. Afterward, the films were transferred to a 100 °C annealing plate and left for 45 min to allow optimum crystallization. After cooling to room temperature, a solution of *x*-XPEAI diluted in IPA (10 mg/1 mL) was spin-coated on the substrate at 4000 rpm for 15 s. Then, The HTM solution was prepared by mixing a stock solution of *spiro*-OMeTAD in chlorobenzene with solutions of *t*-BP, Li-TFSI, and Co(*t*-BuPyPz)₃ (TFSI)₃ (FK209, Dyesol) in acetonitrile with a molar ratio of *spiro*-OMeTAD: FK209:Li(TFSI):*t*-BP at 1:0.03:0.5:3.3. 40 μL of the *spiro*-OMeTAD solution was deposited at 4000 rpm for 20 s on the perovskite film as the hole-transport layer. Finally, a 70 nm-thick gold (Au) layer was thermally evaporated as a counter electrode to complete the device fabrication.

Film Cell Characterization: The morphology and particle size of obtained samples were investigated by using a scanning electron microscope (FEI Sirion-200). 1D XRD analysis was carried out (D8 Advance diffractometer, Bruker) with Cu K α radiation by measuring the diffraction angle (2θ) from 3° to 60°. Grazing incidence wide-angle X-ray scattering (GI-WAXS) patterns represented in reciprocal lattice space were conducted at beamline BL46XU of SPring-8. The sample was irradiated with an X-ray energy of 12.39 keV ($\lambda = 1 \text{ \AA}$) at a fixed incident angle on the order of 0.12°, 0.4° and 2.0° through a Huber diffractometer. The GIWAXS patterns were recorded with a 2D image detector (Pilatus 300 K).

Photoluminescence spectroscopy measurements (PerkinElmer LS 55) were carried out from the film side with an excitation wavelength of 450 nm. TRPL spectroscopy analysis (HORIBA) was performed using a Fluorolog TCSPC with an excitation wavelength of 640 nm. The carrier lifetime was calculated by using the following Equation (1) with a biexponential decay function:

$$R(t) = A1e^{-\frac{t}{\tau1}} + A2e^{-\frac{t}{\tau2}} \quad (1)$$

UV-vis absorption spectra (PerkinElmer) were obtained using a lambda 950S with an integrating sphere.

Computational Details: Density functional theory (DFT) with Perdew-Burke-Ernzerhof (PBE)^[66] density functional along with Grimme's D3 dispersion correction^[67] was used to model the interfaces of FAPbI₃ and (*x*-XPEA)₂PbI₄, where X stands for F, Cl, Br, and *x* for *ortho*, *meta*, *para*, fully relaxing both atomic positions and cell parameters. The wavefunctions were described using the DZVP-MOLOPT^[68] basis set, while the charge density was expanded in the auxiliary plane wave basis set with the 600 Ry cutoff. Core region and core-valence interactions were described with the Goedecker-Teter-Hutter (GHT) pseudopotentials.^[69] The first Brillouin zone was sampled in the Γ -point. The interaction between *x*-XPEA⁺ cations and perovskite surfaces were assessed using Born-Oppenheimer molecular dynamics (BOMD) simulations with 1 fs timestep and the constant temperature of 343 K maintained using the velocity rescaling algorithm. All the simulations were accomplished with the CP2K code.^[70] The structures are visualized using VESTA^[71] and VMD^[72] software.

Solar Cell Characterization: Solar cell measurements were performed using an Oriel solar simulator (450 W xenon, AAA class) and a Keithley model 2400 digital source meter at room temperature. The light intensity was calibrated, and the solar cells' current density-voltage (J - V) characteristics were obtained under the same conditions reported in the previous work. The active areas of solar cells were masked with a metal aperture of 0.09 cm^2 to reduce the influence of the scattered light. The voltage scan rate was 100 mV s^{-1} with no device preconditioning. The EQEs were measured with an IQE 200B (Oriel) for devices without bias light. The long-term stability test was performed as maximum power tracking under 100 mW cm^{-2} illumination with a LED power source, encapsulating samples in a measurement box purged with nitrogen gas kept at $25\text{ }^\circ\text{C}$ by a cooling system.

Supporting Information

Supporting Information is available from the Wiley Online Library or from the author.

Acknowledgements

Z.G.K., A.K., U.G., and X.-X.G. contributed equally to this work. This work was funded by TUBITAK (20AG002). The authors thank Konstantin Tsoi (ODTÜ-GÜNAM) for assisting with electrical simulations provided in Figure S13.

Open access funding provided by Ecole Polytechnique Federale de Lausanne.

Conflict of Interest

A patent application related to materials and their use in PSCs was submitted on 29/11/2022, application number: TR2022/018067.

Data Availability Statement

The data that support the findings of this study are available in the supplementary material of this article.

Keywords

3D/2D perovskite solar cells, phenylethylammonium cations, power conversion efficiency, stability, substituent and position effects

Received: June 27, 2023

Revised: August 28, 2023

Published online:

- [1] National Renewable Energy Laboratory Best Research-Cell Efficiency Chart, <https://www.nrel.gov/pv/cell-efficiency.html> (accessed: May 2023).
- [2] A. Krishna, S. Gottis, M. K. Nazeeruddin, F. Sauvage, *Adv. Funct. Mater.* **2019**, *29*, 1806482.
- [3] Z. Guo, A. K. Jena, G. M. Kim, T. Miyasaka, *Energy Environ. Sci.* **2022**, *15*, 3171.
- [4] T. Wang, W. Deng, J. Cao, F. Yan, *Adv. Energy Mater.* **2022**, *13*, 2201436.
- [5] J. Burschka, N. Pellet, S.-J. Moon, R. Humphry-Baker, P. Gao, M. K. Nazeeruddin, M. Grätzel, *Nature* **2013**, *499*, 316.
- [6] Q. Jiang, Y. Zhao, X. Zhang, X. Yang, Y. Chen, Z. Chu, Q. Ye, X. Li, Z. Yin, J. You, *Nat. Photonics* **2019**, *13*, 460.

- [7] T. Campos, P. Dally, S. Gbegnon, A. Blaizot, G. Trippé-Allard, M. Provost, M. Bouttemy, A. Duchatelet, D. Garrot, J. Rousset, E. Deleporte, *J. Phys. Chem. C* **2022**, *126*, 13527.
- [8] D. T. Gangadharan, D. Ma, *Energy Environ. Sci.* **2019**, *12*, 2860.
- [9] Y. Qin, H. Zhong, J. J. Intemann, S. Leng, M. Cui, C. Qin, M. Xiong, F. Liu, A. K. Y. Jen, K. Yao, *Adv. Energy Mater.* **2020**, *10*, 201904050.
- [10] N. Zhou, H. Zhou, *Small Struct.* **2022**, *3*, 2100232.
- [11] P. Gao, A. R. B. M. Yusoff, M. K. Nazeeruddin, *Nat. Commun.* **2018**, *9*, 5028.
- [12] F. Hu, Y. H. Lou, Z. K. Wang, *Adv. Funct. Mater.* **2023**, 2304848.
- [13] U. Gunes, E. B. Celik, C. C. Akgul, M. Koc, M. Ameri, B. E. Uzuner, M. Ghasemi, M. C. Sahiner, I. Yildiz, H. Z. Kaya, S. Yerci, G. Gunbas, *Adv. Funct. Mater.* **2021**, *31*, 2103130.
- [14] C. Fu, Z. Gu, Y. Tang, Q. Xiao, S. Zhang, Y. Zhang, Y. Song, *Angew. Chem., Int. Ed.* **2022**, *61*, 202117067.
- [15] I. Metcalf, S. Sidhik, H. Zhang, A. Agrawal, J. Persaud, J. Hou, J. Even, A. D. Mohite, *Chem. Rev.* **2023**, *123*, 9565.
- [16] X. Zhou, W. Qi, J. Li, J. Cheng, Y. Li, J. Luo, M. J. Ko, Y. Li, Y. Zhao, X. Zhang, *Sol. RRL* **2020**, *4*, 202000107.
- [17] J. Hu, I. W. H. Oswald, S. J. Stuard, M. M. Nahid, N. Zhou, O. F. Williams, Z. Guo, L. Yan, H. Hu, Z. Chen, X. Xiao, Y. Lin, Z. Yang, J. Huang, A. M. Moran, H. Ade, J. R. Neilson, W. You, *Nat. Commun.* **2019**, *10*, 1276.
- [18] H. Su, L. Zhang, Y. Liu, Y. Hu, B. Zhang, J. You, X. Du, J. Zhang, X. Ren, J. Gou, S. Liu, *Nano Energy* **2022**, *95*, 106965.
- [19] X. Ren, B. Zhang, L. Zhang, J. Wen, B. Che, D. Bai, J. You, T. Chen, S. Liu, *ChemSusChem* **2021**, *14*, 3182.
- [20] Z. Wang, Q. Wei, X. Liu, L. Liu, X. Tang, J. Guo, S. Ren, G. Xing, D. Zhao, Y. Zheng, *Adv. Funct. Mater.* **2021**, *31*, 2008404.
- [21] H. B. Lee, N. Kumar, B. Tyagi, K.-J. Ko, J.-W. Kang, *Sol. RRL* **2021**, *5*, 2000589.
- [22] S. Zhao, J. Xie, G. Cheng, Y. Xiang, H. Zhu, W. Guo, H. Wang, M. Qin, X. Lu, J. Qu, J. Wang, J. Xu, K. Yan, *Small* **2018**, *14*, 1803350.
- [23] H. Pan, X. Zhao, X. Gong, Y. Shen, M. Wang, *J. Phys. Chem. Lett.* **2019**, *10*, 1813.
- [24] H. Li, L. Tan, C. Jiang, M. Li, J. Zhou, Y. Ye, Y. Liu, C. Yi, *Adv. Funct. Mater.* **2023**, *33*, 2211232.
- [25] M. Li, J. Zhou, L. Tan, Y. Liu, S. Wang, C. Jiang, H. Li, X. Zhao, X. Gao, W. Tress, L. Ding, C. Yi, *Energy Environ. Mater.* **2022**, *8*, 20207422.
- [26] H. Chen, S. Teale, B. Chen, Y. Hou, L. Grater, T. Zhu, K. Bertens, S. M. Park, H. R. Atapattu, Y. Gao, M. Wei, A. K. Johnston, Q. Zhou, K. Xu, D. Yu, C. Han, T. Cui, E. H. Jung, C. Zhou, W. Zhou, A. H. Proppe, S. Hoogland, F. Laquai, T. Filleter, K. R. Graham, Z. Ning, E. H. Sargent, *Nat. Photonics* **2022**, *16*, 352.
- [27] T. Campos, P. Dally, S. Gbegnon, A. Blaizot, G. Trippé-Allard, M. Provost, M. Bouttemy, A. Duchatelet, D. Garrot, J. Rousset, E. Deleporte, *J. Phys. Chem. C* **2022**, *126*, 13527.
- [28] M. Pei, Q. Dong, M. Wang, Y. Wang, H. Ma, J. Liu, R. Wang, J. Bian, Y. Shi, *ACS Appl. Mater. Interfaces* **2022**, *14*, 16920.
- [29] S. Cacovich, G. Vidon, M. Degani, M. Legrand, L. Gouda, J.-B. Puel, Y. Vaynzof, J.-F. Guillemoles, D. Ory, G. Grancini, *Nat. Commun.* **2022**, *13*, 2868.
- [30] M. Degani, Q. An, M. Albaladejo-Siguan, Y. J. Hofstetter, C. Cho, F. Paulus, G. Grancini, Y. Vaynzof, *Sci. Adv.* **2021**, *49*, eabj7930.
- [31] L. Wang, Q. Zhou, Z. Zhang, W. Li, X. Wang, Q. Tian, X. Yu, T. Sun, J. Wu, B. Zhang, P. Gao, *J. Energy Chem.* **2022**, *64*, 179.
- [32] M. Wang, Y. Yin, W. Cai, J. Liu, Y. Han, Y. Feng, Q. Dong, Y. Wang, J. Bian, Y. Shi, *Adv. Funct. Mater.* **2022**, *32*, 2108567.
- [33] X. Jiang, S. Chen, Y. Li, L. Zhang, N. Shen, G. Zhang, J. Du, N. Fu, B. Xu, *ACS Appl. Mater. Interfaces* **2021**, *13*, 2558.
- [34] G. Liu, H. Zheng, H. Xu, L. Zhang, X. Xu, S. Xu, X. Pan, *Nano Energy* **2020**, *73*, 104753.

- [35] Y. Liu, S. Akin, L. Pan, R. Uchida, N. Arora, J. V. Milic, A. Hinderhofer, F. Schreiber, A. R. Uhl, S. M. Zakeeruddin, A. Hagfeldt, M. I. Dar, M. Grätzel, *Sci. Adv.* **2019**, *5*, eaaw2543.
- [36] P. Li, H. Dong, J. Xu, J. Chen, B. Jiao, X. Hou, J. Li, Z. Wu, *ACS Energy Lett.* **2020**, *5*, 2327.
- [37] N. Yan, Y. Gao, J. Yang, Z. Fang, J. Feng, X. Wu, T. Chen, S. Liu, *Angew. Chem., Int. Ed.* **2023**, *62*, 202216668.
- [38] T. Lin, T. Dai, X. Li, *Sol. RRL* **2023**, *7*, 2201138.
- [39] U. Gunes, F. V. Yaylali, Z. Gozukara Karabag, X.-X. Gao, O. A. Syzgantseva, A. Karabag, G. B. Yildirim, K. Tsoi, N. Shibayama, H. Kanda, A. I. Rafieh, L. Zhong, A. Züttel, P. J. Dyson, S. Yerci, M. K. Nazeeruddin, G. Gunbas, *Cell Rep. Phys. Sci.* **2023**, *4*, 101380.
- [40] D. Li, W.-Y. Lai, Y.-Z. Zhang, W. Huang, *Adv. Mater.* **2018**, *30*, 1704738.
- [41] M.-H. Li, H.-H. Yeh, Y.-H. Chiang, U.-S. Jeng, C.-J. Su, H.-W. Shiu, Y.-J. Hsu, N. Kosugi, T. Ohigashi, Y.-A. Chen, P.-S. Shen, P. Chen, T.-F. Guo, *Adv. Mater.* **2018**, *30*, 1801401.
- [42] M. S. Abbas, S. Hussain, J. Zhang, B. Wang, C. Yang, Z. Wang, Z. Wei, R. Ahmad, *Sustain. Energy Fuels* **2019**, *4*, 324.
- [43] K. T. Cho, S. Paek, G. Grancini, C. Roldán-Carmona, P. Gao, Y. Lee, M. K. Nazeeruddin, *Energy Environ. Sci.* **2017**, *10*, 621.
- [44] T. Zhou, H. Lai, T. Liu, D. Lu, X. Wan, X. Zhang, Y. Liu, Y. Chen, *Adv. Mater.* **2019**, *31*, 1901242.
- [45] A. H. Proppe, A. Johnston, S. Teale, A. Mahata, R. Quintero-Bermudez, E. H. Jung, L. Grater, T. Cui, T. Filleter, C.-Y. Kim, S. O. Kelley, F. De Angelis, E. H. Sargent, *Nat. Commun.* **2021**, *12*, 3472.
- [46] C. Liu, Y. Yang, K. Rakstys, A. Mahata, M. Franckevicius, E. Mosconi, R. Skackauskaite, B. Ding, K. G. Brooks, O. J. Usiobo, J.-N. Audinot, H. Kanda, S. Driukas, G. Kavaliauskaite, V. Gulbinas, M. Dessimoz, V. Getautis, F. De Angelis, Y. Ding, S. Dai, P. J. Dyson, M. K. Nazeeruddin, *Nat. Commun.* **2021**, *12*, 6394.
- [47] R. Quintero-Bermudez, A. Gold-Parker, A. H. Proppe, R. Munir, Z. Yang, S. O. Kelley, A. Amassian, M. F. Toney, E. H. Sargent, *Nat. Mater.* **2018**, *17*, 900.
- [48] F. Wang, X. Jiang, H. Chen, Y. Shang, H. Liu, J. Wei, W. Zhou, H. He, W. Liu, Z. Ning, *Joule* **2018**, *2*, 2732.
- [49] G. Wu, R. Liang, M. Ge, G. Sun, Y. Zhang, G. Xing, *Adv. Mater.* **2022**, *34*, 2105635.
- [50] Y. Lv, X. Song, Y. Yin, Y. Feng, H. Ma, C. Hao, S. Jin, Y. Shi, *ACS Appl. Mater. Interfaces* **2020**, *12*, 698.
- [51] S. Zouhair, S.-M. Yoo, D. Bogachuk, J. P. Herterich, J. Lim, H. Kanda, B. Son, H. J. Yun, U. Würfel, A. Chahboun, M. K. Nazeeruddin, A. Hinsch, L. Wagner, H. Kim, *Adv. Energy Mater.* **2022**, *12*, 2200837.
- [52] H.-S. Choi, H.-S. Kim, *Materials* **2020**, *13*, 3868.
- [53] P. Chen, Y. Bai, S. Wang, M. Lyu, J.-H. Yun, L. Wang, *Adv. Funct. Mater.* **2018**, *28*, 1706923.
- [54] J. Zhuang, P. Mao, Y. Luan, X. Yi, Z. Tu, Y. Zhang, Y. Yi, Y. Wei, N. Chen, T. Lin, F. Wang, C. Li, J. Wang, *ACS Energy Lett.* **2019**, *4*, 2913.
- [55] X. Yue, X. Zhao, B. Fan, Y. Yang, L. Yan, S. Qu, H. Huang, Q. Zhang, H. Yan, P. Cui, J. Ji, J. Ma, M. Li, *Adv. Funct. Mater.* **2023**, *33*, 2209921.
- [56] M. A. Mahmud, H. T. Pham, T. Duong, Y. Yin, J. Peng, Y. Wu, W. Liang, L. Li, A. Kumar, H. Shen, D. Walter, H. T. Nguyen, N. Mozaffari, G. D. Tabi, G. Andersson, K. R. Catchpole, K. J. Weber, T. P. White, *Adv. Funct. Mater.* **2021**, *31*, 2104251.
- [57] H. Kim, S.-U. Lee, D. Y. Lee, M. J. Paik, H. Na, J. Lee, S. I. Seok, *Adv. Energy Mater.* **2019**, *9*, 1902740.
- [58] S. Tan, N. Zhou, Y. Chen, L. Li, G. Liu, P. Liu, C. Zhu, J. Lu, W. Sun, Q. Chen, H. Zhou, *Adv. Energy Mater.* **2019**, *9*, 1803024.
- [59] H. Tan, Q. Lyu, Z. Xie, M. Li, K. Wang, K. Wang, B. Xiong, L. Zhang, J. Zhu, *Adv. Mater.* **2019**, *31*, 1805496.
- [60] G. Grancini, M. K. Nazeeruddin, *Nat. Rev. Mater.* **2019**, *4*, 4.
- [61] Q. Zhou, B. Liu, X. Shai, Y. Li, P. He, H. Yu, C. Chen, Z.-X. Xu, D. Wei, J. Chen, *Chem. Commun.* **2023**, *59*, 4128.
- [62] C. Chen, J. Liang, J. Zhang, X. Liu, X. Yin, H. Cui, H. Wang, C. Wang, Z. Li, J. Gong, Q. Lin, W. Ke, C. Tao, B. Da, Z. Ding, X. Xiao, G. Fang, *Nano Energy* **2021**, *90*, 106608.
- [63] Z. Qin, H. Xue, M. Qin, Y. Li, X. Wu, W.-R. Wu, C.-J. Su, G. Brocks, S. Tao, X. Lu, *Small* **2023**, *19*, 2206787.
- [64] L. Liang, H. Luo, J. Hu, H. Li, P. Gao, *Adv. Energy Mater.* **2020**, *10*, 2000197.
- [65] C. Hansch, A. Leo, R. W. Taft, *Chem. Rev.* **1991**, *91*, 165.
- [66] J. P. Perdew, K. Burke, M. Ernzerhof, *Phys. Rev. Lett.* **1996**, *77*, 3865.
- [67] S. Grimme, J. Antony, S. Ehrlich, H. Krieg, *ChemPhysChem* **2010**, *132*, 3414.
- [68] J. Vandevondele, J. Hutter, *J. Chem. Phys.* **2007**, *127*, 114105.
- [69] S. Goedecker, M. Teter, J. Hutter, *Phys. Rev. B* **1996**, *54*, 1703.
- [70] T. D. Kühne, M. Iannuzzi, M. Del Ben, V. V. Rybkin, P. Seewald, F. Stein, T. Laino, R. Z. Khaliullin, O. Schütt, F. Schiffmann, D. Golze, J. Wilhelm, S. Chulkov, M. H. Bani-Hashemian, V. Weber, U. Borstnik, M. Taillefumier, A. S. Jakobovits, A. Lazzaro, H. Pabst, T. Müller, R. Schade, M. Guidon, S. Andermatt, N. Holmberg, G. K. Schenter, A. Hehn, A. Bussy, F. Belleflamme, G. Tabacchi, et al., *J. Chem. Phys.* **2020**, *152*, 194103.
- [71] K. Momma, F. Izumi, *J. Appl. Crystallogr.* **2011**, *44*, 1272.
- [72] W. Humphrey, A. Dalke, K. Schulten, *J. Mol. Graphics* **1996**, *14*, 33.